eng

MDPI

Article

Respiration and Heartbeat Detection Using FMCW Radar Based on Secondary Variational Mode Decomposition

Zeyan Yu [1], Yuhang Yin [1], Yunfan Chen [1], Qinghua Cui [2] and Xiangkui Wan [1,*]

[1] Hubei Key Laboratory for High-Efficiency Utilization of Solar Energy and Operation Control of Energy Storage System, Hubei University of Technology, Wuhan 430068, China; y1508257944@163.com (Z.Y.)
[2] School of Sports Medicine, Wuhan Sports University, Wuhan 430079, China
* Correspondence: xkwan@hbut.edu.cn

Abstract

In non-contact respiration and heartbeat detection using FMCW millimeter-wave radar, the effectiveness of signal separation directly determines the final detection accuracy. Traditional methods suffer from reliance on manual experience, inadequate suppression of high-order respiratory harmonics, and poor adaptability to complex environments. This paper proposes a signal separation algorithm based on Secondary Variational Mode Decomposition (SVMD). The Grey Wolf Algorithm (GWA) is used to adaptively select the key parameters of VMD for rough signal separation. After Wavelet Packet Decomposition (WPD), secondary VMD is applied to suppress high-order respiratory harmonics in the heartbeat signal, thereby achieving refined separation of respiration and heartbeat signals. Experimental results show that the proposed method achieves a detection accuracy of no less than 95.59% for both respiration and heartbeat in four scenarios, with a mean absolute error lower than that of traditional methods. The 95% Bland–Altman limits of agreement comply with the clinically referenced AAMI device accuracy expectations, demonstrating the high accuracy and strong stability of the proposed method.

Keywords: FMCW radar; respiration and heartbeat detection; respiration and heartbeat signal separation; SVMD

1. Introduction

In recent years, with the accelerating aging of the global population, health problems such as cardiovascular diseases, sleep apnea syndrome, and chronic respiratory diseases have become worldwide public health challenges. The World Health Organization (WHO) has repeatedly emphasized that respiration and heartbeat, as two core vital signs reflecting human cardiopulmonary function, are critically important for early disease warning, intensive care, sleep health assessment, and emergency intervention [1]. Therefore, developing a technology capable of long-term, continuous, non-invasive, and accurate respiration and heartbeat detection is of urgent practical significance for ensuring the safety of high-risk groups and improving their quality of life and independent living ability.

Human respiration and heartbeat detection technologies are generally divided into two categories: contact and non-contact. Traditional contact detection technologies have three inherent limitations: they are unsuitable for burn patients or certain special populations [2], interfere with users' normal sleep and daily activities [3], and are not widely accessible [4]. Thus, they are not applicable for long-term health monitoring in homes and communities. Consequently, developing non-contact, highly reliable, and robust respiration

Check for updates

Academic Editor: Sergio Spanò

Received: 20 September 2026
Revised: 31 October 2026
Accepted: 1 November 2026
Published: 5 November 2026

Copyright: © 2026 by the authors. Licensee MDPI, Basel, Switzerland. This article is an open access article distributed under the terms and conditions of the Creative Commons Attribution (CC BY) license.

and heartbeat detection technology has become a common research direction in intelligent medical treatment and health monitoring.

Among numerous non-contact detection technologies, radar echo detection is insensitive to environmental factors, can penetrate common furniture and clothing, and allows radar antennas to be concealed [5], making it an ideal approach for continuous, unobtrusive, and accurate detection. Among all bio-radars for respiration and heartbeat monitoring, Frequency Modulated Continuous Wave (FMCW) radar stands out due to its unique advantages. Compared with Continuous Wave (CW) radar, FMCW radar has stronger anti-clutter interference capability; compared with Ultra-Wide Band (UWB) radar, it has lower hardware complexity. FMCW radar achieves the best balance among detection performance, environmental robustness, and system implement ability [6].

Given these advantages, non-contact respiration and heartbeat detection using FMCW radar has attracted increasing attention in recent years. The core problem lies in accurately extracting respiration and heartbeat signals from complex echo signals containing respiration, heartbeat, and clutter. Early signal separation mainly relied on fixed-band filtering methods. In 2009, Lin et al. [7] used band-pass filters to preliminarily separate respiration, heartbeat, and clutter by presetting frequency bands. However, respiration and heartbeat signals are non-stationary physiological signals, so manually preset frequency bands lead to poor separation. In 2014, Xu et al. [8] first applied Empirical Mode Decomposition (EMD) to radar respiration and heartbeat signal processing. EMD is adaptive and decomposes signals according to their intrinsic time scales, but it suffers from inherent mode mixing and end effects, which limit stability under low signal-to-noise ratio conditions.

To address these issues, Dragomiretskiy and Zosso proposed Variational Mode Decomposition (VMD) in 2014, which achieves robust decomposition through a variational framework and significantly suppresses mode mixing [9]. In 2015, Islam et al. [10] first applied VMD to radar respiration and heartbeat signal separation, verifying its effectiveness. However, the mode number and penalty factor of VMD still depend on manual selection; inappropriate parameters cause over-decomposition or under-decomposition. Recent research has focused on integrating multiple methods for refined processing and exploring new solutions beyond traditional frameworks. In 2023, Qu et al. [11] proposed a parameter-adaptive VMD algorithm, which adaptively determines key VMD parameters by introducing an optimization algorithm, reducing dependence on prior knowledge and improving parameter selection accuracy. Nevertheless, this method cannot suppress the interference of residual respiratory high-order harmonics in heartbeat signals. In 2025, Liu et al. [12] proposed an algorithm cascade framework, effectively suppressing clutter interference in complex environments through a two-stage strategy of "removing deterministic strong interference first, then suppressing random noise".

To address the above problems in signal separation—reliance on manual parameter presetting leading to over/under-decomposition, inability to suppress respiratory high-order harmonics, and low purity of weak heartbeat signal separation—this paper proposes a respiration and heartbeat signal separation algorithm based on Secondary Variational Mode Decomposition (SVMD). The algorithm integrates Grey Wolf Algorithm Improved VMD (GWAIVMD) and SVMD to obtain purer respiration and heartbeat signals. System tests in four scenarios verify the high accuracy and strong stability of the proposed algorithm in FMCW radar respiration and heartbeat detection.

2. Principle of FMCW Radar Respiration and Heartbeat Detection

FMCW radar generates chirp signal with linearly varying frequency over time through a synthesizer and transmits it via a transmit antenna (TX). The signal is blocked and reflected by objects such as the human chest in its path. The radar receives the reflected chirp signal

through a receive antenna (RX). The transmitted signal and the received reflected signal are mixed in a mixer to generate an Intermediate Frequency (*IF*) signal containing target information. For two sinusoidal input signals of the mixer, the IF signal is expressed as:

$$x_{IF} = Asin(2\pi S\tau t + 2\pi fc \cdot \tau) \quad (1)$$

where $S = \frac{B}{Tc}$ is the chirp slope, B is the bandwidth, Tc is the duration of the chirp signal, $\tau = \frac{2R}{c}$ is the time delay from signal transmission to reception, R is the distance between radar and target, and fc is the initial carrier frequency.

The frequency of the generated IF signal is constant over time. The relationship between the distance R between the FMCW radar and the target and the IF signal frequency f_{IF} is:

$$R = \frac{c \cdot f_{IF}}{2s} \quad (2)$$

Thus, measuring the *IF* signal frequency yields the distance between the radar and the target.

The range resolution d_{res} of FMCW radar refers to the minimum distance difference by which the radar system can distinguish two or more adjacent targets [13]. For two stationary targets with a distance difference ΔR, the frequency difference Δf between the two *IF* signals is:

$$\Delta f = \frac{2S\Delta R}{c} \quad (3)$$

The radar receives a mixed *IF* signal that is the superposition of *IF* signals reflected by two different objects. To distinguish the two *IF* signals in the frequency domain, their frequency difference Δf must exceed the frequency resolution. According to the discrete Fourier transform theory, the frequency resolution of a signal with duration *Tc* is the reciprocal of time [14], yielding the range resolution of FMCW radar:

$$_{res} = \frac{c}{2B} \quad (4)$$

It can be seen that the range resolution of the radar is only related to the bandwidth of the transmitted signal.

This paper uses FMCW radar to detect human respiration and heartbeat. The detection is based on measuring the chest displacement amplitude caused by respiration and heartbeat, using the relationship between the IF signal and the distance between the object and the radar.

Table 1 shows the chest displacement amplitude and frequency of respiration and heartbeat signals caused by human physiological activities. Since the micro-motion signals caused by respiration and heartbeat are at the millimeter or sub-millimeter level, traditional low-frequency radars often lack accuracy in solving such problems. This paper selects a 60 GHz FMCW millimeter-wave radar with a bandwidth of 4 GHz. According to Equation (4), the radar range resolution is 37.5 mm, much larger than the chest displacement amplitude caused by respiration and heartbeat listed in Table 1. However, continuously increasing the bandwidth of the transmitted signal greatly increases the system cost, hardware complexity, and power consumption of the radar, which is unrealistic in engineering [15]. From Equation (1), the phase difference Δf_{IF} of the *IF* signal when the radar measures human respiration and heartbeat is:

$$\Delta f_{IF} = 2\pi\tau \cdot f_c = 4\pi \cdot \Delta R \cdot \frac{f_c}{c} = \frac{4\pi}{\lambda} \cdot \Delta R \quad (5)$$

Table 1. Parameter model of human respiration and heartbeat signals.

Vital Sign Signal	Amplitude	Frequency
Respiration signal	1~12 mm	0.1~0.5 Hz
Heartbeat signal	0.5~1 mm	0.8~2.5 Hz

The wavelength λ of the 60 GHz FMCW millimeter-wave radar used in this paper is 5 mm. Combined with Table 1 and Equation (5), a displacement of 1 mm produces a phase change of approximately 144°. Although the tiny chest displacement caused by respiration and heartbeat is much smaller than the radar range resolution, converting this distance change into a phase change is highly sensitive.

The complete process of respiration and heartbeat detection based on FMCW radar is shown in Figure 1.

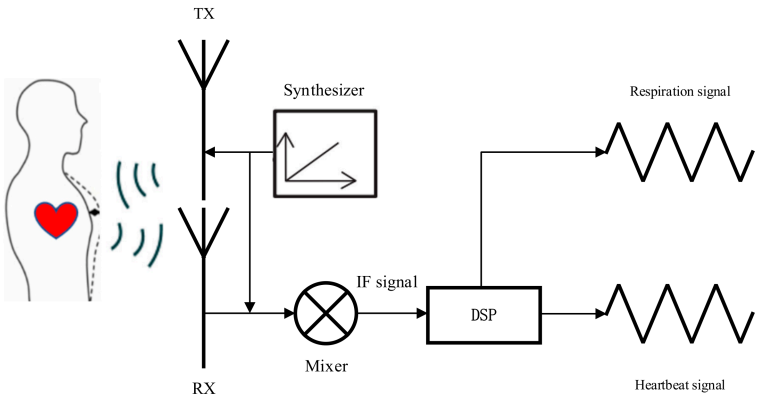


Figure 1. Flowchart of Respiration and Heartbeat Detection Using FMCW Radar.

The 60 GHz FMCW millimeter-wave radar transmits a chirp signal through a synthesizer. After being blocked and reflected by the human chest, the signal is mixed with the transmitted chirp signal in the mixer to generate an IF signal, which contains the tiny chest displacement difference caused by human respiration and heartbeat activities. After the IF signal is processed by a Digital Signal Processor (DSP), the tiny and insensitive displacement difference is converted into an obvious phase difference to detect human respiration and heartbeat signals, which is the core principle of FMCW radar for detecting human respiration and heartbeat signals.

3. Respiration and Heartbeat Detection Based on Refined Signal Separation Algorithm

According to the aforementioned principle of FMCW radar detecting, after obtaining the IF signal from the mixer, the phase signal must first be extracted. Then, signal separation and frequency estimation are performed to obtain the respiration and heartbeat signals and estimate their frequencies. The complete algorithm flow for measuring human respiration and heartbeat based on FMCW millimeter-wave radar is shown in Figure 2.

In the signal preprocessing stage, static clutter is first removed from the IF signal. After Range-Dimensional Fast Fourier Transform (Range-FFT), phase extraction and phase unwrapping are performed. Respiration and heartbeat signal separation is then achieved through two steps: rough separation and refined separation. Finally, frequency estimation is performed on the separated signals to complete detection.

After static clutter filtering, phase extraction, and unwrapping, the phase signal is still a mixture of respiration, heartbeat, and residual clutter. Accurately separating pure

respiration and heartbeat components from this composite signal is the key prerequisite for subsequent frequency estimation. Traditional signal separation methods are mainly divided into two categories: fixed-band filtering separation (e.g., band-pass filters), which relies on preset parameters and struggles to adapt to individual differences; and adaptive mode decomposition (e.g., EMD, VMD), which decompose signals according to their characteristics but suffer from mode mixing and manual parameter dependence.

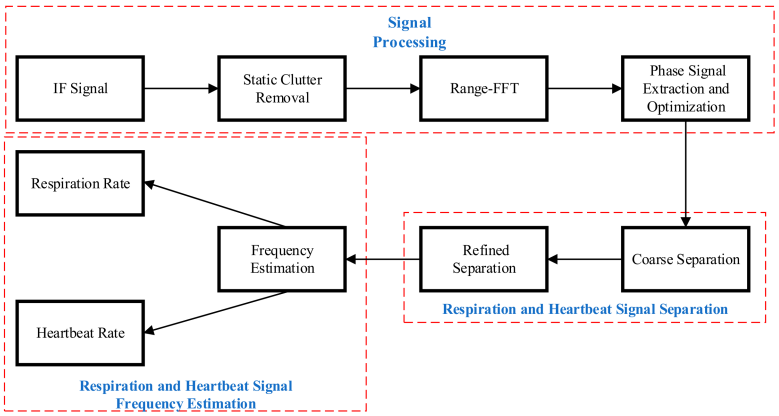


Figure 2. Flowchart of FMCW Radar Algorithm for Respiration and Heartbeat Detection.

To address these limitations, this chapter proposes a respiration and heartbeat signal separation algorithm based on SVMD, which avoids blind parameter tuning, suppresses the influence of respiratory high-order harmonics on heartbeat signals, and accurately separates respiration, heartbeat, and residual noise. The complete flow of the SVMD-based separation algorithm is shown in Figure 3.

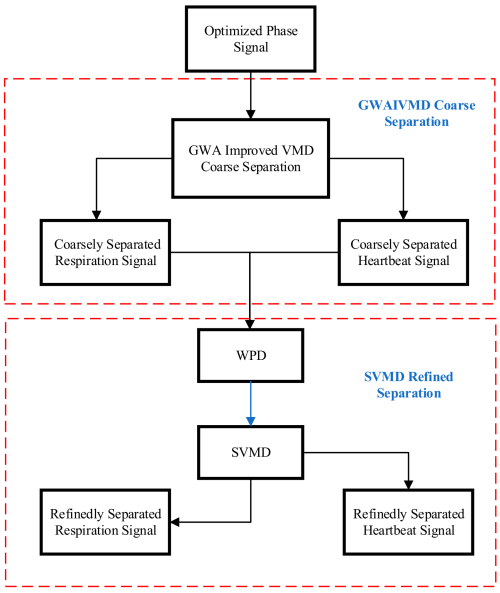


Figure 3. Flowchart of the SVMD-based Signal Separation Algorithm Detection.

As shown in the flow chart of the SVMD-based respiration and heartbeat signal separation algorithm, the method first uses the Grey Wolf Algorithm (GWA) with envelope entropy as the fitness function to adaptively search for the optimal mode number K and penalty factor α in VMD. Then the GWAIVMD algorithm is used for rough separation of the phase signal, and respiration and heartbeat candidate modes are selected according to the central frequency of the modes after rough separation. The roughly separated signal is separated via Wavelet Packet Decomposition (WPD). Finally, the SVMD algorithm is used

to suppress the interference of respiratory high-order harmonics in the heartbeat signal, obtaining refined respiration and heartbeat signals.

3.1. Rough Signal Separation Based on GWAIVMD

GWA is an optimization algorithm inspired by the social hierarchy and hunting behavior of grey wolf packs. Grey wolves have a strict social hierarchy, which GWA maps to candidate solutions in the optimization process, as shown in Table 2.

Table 2. Correspondence between grey wolf hierarchy and algorithm roles.

Grey Wolf Rank	Algorithm Role	Optimization Meaning
α (leader)	Optimal	Responsible for decision-making, the best candidate solution in the current population
β	Suboptimal	Assists the leader; can replace the leader if missing
δ	Third optimal	Obey α and β, dominates lower-ranking individuals
ω (lowest)	Remaining	Balances internal relations, follows the top three

The three individuals with the best fitness in the current population are marked as α, β, and δ, and the rest are ω. The search for the optimal solution is guided by α, β, and δ, while ω follows and updates positions.

Grey wolves first encircle prey during hunting, defined as:

$$\vec{D} = \left|\vec{C} \cdot \vec{X}_P(t) - \vec{X}(t)\right| \tag{6}$$

$$\vec{X}(t+1) = \vec{X}_P(t) - \vec{A} \cdot \vec{D} \tag{7}$$

where $\vec{X}_P(t)$ is the prey position, $\vec{X}(t)$ is the grey wolf individual position, and t is the iteration number. The absolute value of control parameter $\vec{A}$ determines whether the wolf approaches ($\left|\vec{A}\right| < 1$) or moves away ($\left|\vec{A}\right| > 1$) from the prey, balancing local and global exploration. Control parameter $\vec{C}$ enhances search randomness via random weighting to avoid local optima. Since the prey position is unknown, GWA assumes α, β, and δ have better knowledge of the prey location. It first calculates distances between other wolves and α, β, and δ, then updates positions under their guidance. The final position is the average of the three guidance terms, driving wolves toward the optimal region. GWA has advantages such as few parameters, fast convergence, and strong global search capability, and has been widely used in various engineering optimization problems. Each candidate parameter set $[K, \alpha]$ of VMD corresponds to an individual in the grey wolf pack. GWA searches for the optimal individual position (i.e., optimal parameter solution $[K_{best}, \alpha_{best}]$) within the search space to maximize the fitness function value of VMD signal separation, yielding the best signal quality.

The flowchart of GWA adaptively searching for optimal VMD parameters is shown in Figure 4. According to the frequency ranges of respiration and heartbeat signals, combined with the signal sampling rate, amplitude characteristics, and multiple experimental results, the search range of VMD mode number K is preset to $[2, 10]$, and the penalty factor α to $[200, 5000]$. First, N grey wolf individuals ($N = 20$ in this paper) are randomly generated in the search space, each position represented by a parameter set $[K, \alpha]$ (K integer, α continuous). Initialize iteration counter t = 1, maximum iterations T = 30. For each individual, the current position is input into VMD to decompose the signal into K modes, then calculate the fitness function value of each mode. For quasi-periodic physiological signals such as respiration and heartbeat, pure signal components exhibit regular envelope shapes. To ensure consistency between the optimization strategy of the algorithm and the definition of the fitness function, this paper adopts the reciprocal of envelope entropy as the

fitness index: the smaller the envelope entropy, the larger the fitness function value, and the purer the decomposed mode components.

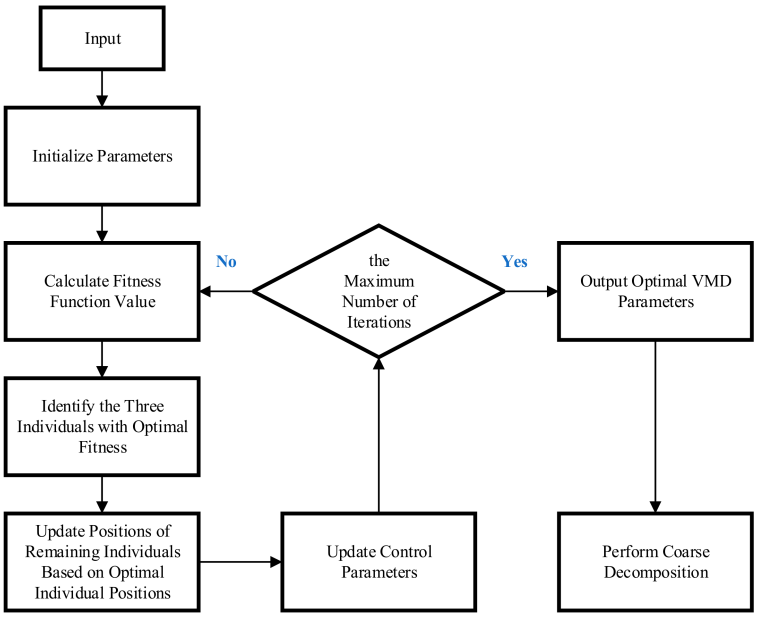


Figure 4. Flowchart of the GWA for Adaptive Search of Optimal VMD Parameters.

For the i mode function $u_i(t)$ separated by VMD, the envelope entropy calculation steps are:

(1): Perform Hilbert transform on $u_i(t)$ to obtain the analytic signal $z_i(t)$:

$$z_i(t) = u_i(t) + j \cdot H[u_i(t)] \tag{8}$$

where $H[u_i(t)]$ denotes the Hilbert transform of $u_i(t)$.

(2): Extract the instantaneous envelope $e_i(t)$:

$$e_i(t) = |z_i(t)| \tag{9}$$

(3): Normalize the envelope sequence to obtain the probability distribution $P_i(j)$:

$$p_i(j) = \frac{e_i(j)}{\sum_{j=1}^{N} e_i(j)} \tag{10}$$

where N is the signal length.

(4): Calculate the envelope entropy H_{env}(i) of the mode:

$$H_{env}(i) = -\sum_{j=1}^{N} p_i(j) log_2 p_i(j) \tag{11}$$

For a given parameter set $[K, \alpha]$, VMD decomposes the signal into K modes. The reciprocal of the average envelope entropy of all modes is taken as the fitness value corresponding to this parameter set:

$$F(k, \alpha) = \left[\frac{1}{k} \sum_{i=1}^{k} H_{env}(i) \right]^{-1} \tag{12}$$

$F(K,\alpha)$ is the fitness function value under this parameter. The grey wolf population is sorted by fitness value; the top three individuals are marked as α, β, and δ, and the rest as ω. According to the GWA hunting mechanism, all individual positions and control parameters are updated based on α, β, and δ. Finally, check whether the maximum iteration is reached:

if $t \leq T$, return to iterate; otherwise, terminate the algorithm and output the current α position $[K_{best}, \alpha_{best}]$ as the optimal VMD parameters.

After obtaining the optimal parameters $[K_{best}, \alpha_{best}]$ via GWA adaptive search, they are input into the VMD algorithm to decompose the extracted phase signal into K_{best} Intrinsic Mode Functions (IMFs), denoted $u_1(t)$, $u_2(t)$..., $u_{best}(t)$. According to VMD principles, each IMF has a central frequency, sorted from low to high: $u_1(t)$ corresponds to the lowest frequency component, $u_{best}(t)$ to the highest. After VMD decomposition, is obtained the central frequency of each IMF. Based on prior knowledge in Table 1, they are divided into two candidate mode sets: the respiration mode candidate set M_b, obtain all modes with central frequency 0.1~0.5 Hz; heartbeat mode candidate set M_h, obtain all modes with central frequency 0.8~2.5 Hz. Modes outside these ranges are discarded. Linearly superpose all modes in the respiration and heartbeat candidate sets to obtain roughly separated respiration and heartbeat signals:

$$s'_B(t) = \sum_{u_k \in M_B} u_k(t) \tag{13}$$

$$s'_R(t) = \sum_{u_k \in M_R} u_k(t) \tag{14}$$

where $s'_B(t)$ and $s'_R(t)$ are the roughly separated respiration and heartbeat signals, respectively, and u_k is the mode function.

The rough separation stage fully utilizes VMD static frequency band division to extract the main respiration and heartbeat components from the complex mixture, reducing subsequent processing complexity. However, roughly separated signals may still contain random noise, frequency band overlap, and residual respiratory high-order harmonics in heartbeat signals. Thus, refined separation of roughly separated respiration and heartbeat signals is required.

3.2. Refined Signal Separation Based on SVMD

WPD is an extension of wavelet transform. Unlike wavelet transform, which only decomposes low-frequency components layer by layer, WPD decomposes both high- and low-frequency components of each layer, forming a uniform binary tree structure across the entire frequency band [16]. This decomposition enables finer frequency band division, especially suitable for extracting weak high-frequency signals such as heartbeat. For a raw signal with sampling frequency f_s, the frequency range f_j of each sub-band at layer j is:

$$f_j = \left[\frac{l \cdot f_s}{2^{j+1}}, \frac{(l+1) \cdot f_s}{2^{j+1}} \right], l \in \left[0, 2^j - 1\right] \tag{15}$$

The decomposition layer j determines the fineness of frequency band division. Too few layers lead to coarse division and poor separation of aliased components; too many layers increase computation and may introduce boundary effects. The signal sampling frequency f_s in this paper is 20 Hz. According to the Nyquist theorem, the effective analysis range is 0~10 Hz. Combined with the respiration and heartbeat frequency bands, the decomposition layer j = 3 is finally selected. When j = 2, the respiration and heartbeat bands overlap in the frequency domain, hindering effective separation, resulting in severe frequency estimation bias and degraded accuracy. When j = 4, boundary effects arise, which increases the MAE of the estimated respiration and heartbeat frequencies.

The choice of wavelet basis function directly affects decomposition performance. Common bases include Daubechies (db) and Symlet (sym) series. The db series has orthogonality, compact support, and good regularity, and is widely used in biomedical signal processing [17]. Considering waveform characteristics of respiration and heartbeat

signals and computational complexity, db5 wavelet is selected as the basis function for signal separation.

However, due to frequency band overlap between heartbeat signals and respiratory high-order harmonics, heartbeat signals separated by three-layer WPD still contain interference from respiratory high-order harmonics. To obtain purer heartbeat signals, this section proposes a refined separation algorithm based on SVMD, combining energy distribution to perform SVMD on the WPD-separated signals, finally yielding refined respiration and heartbeat signals. The complete flow of the SVMD-based refined separation is shown in Figure 5.

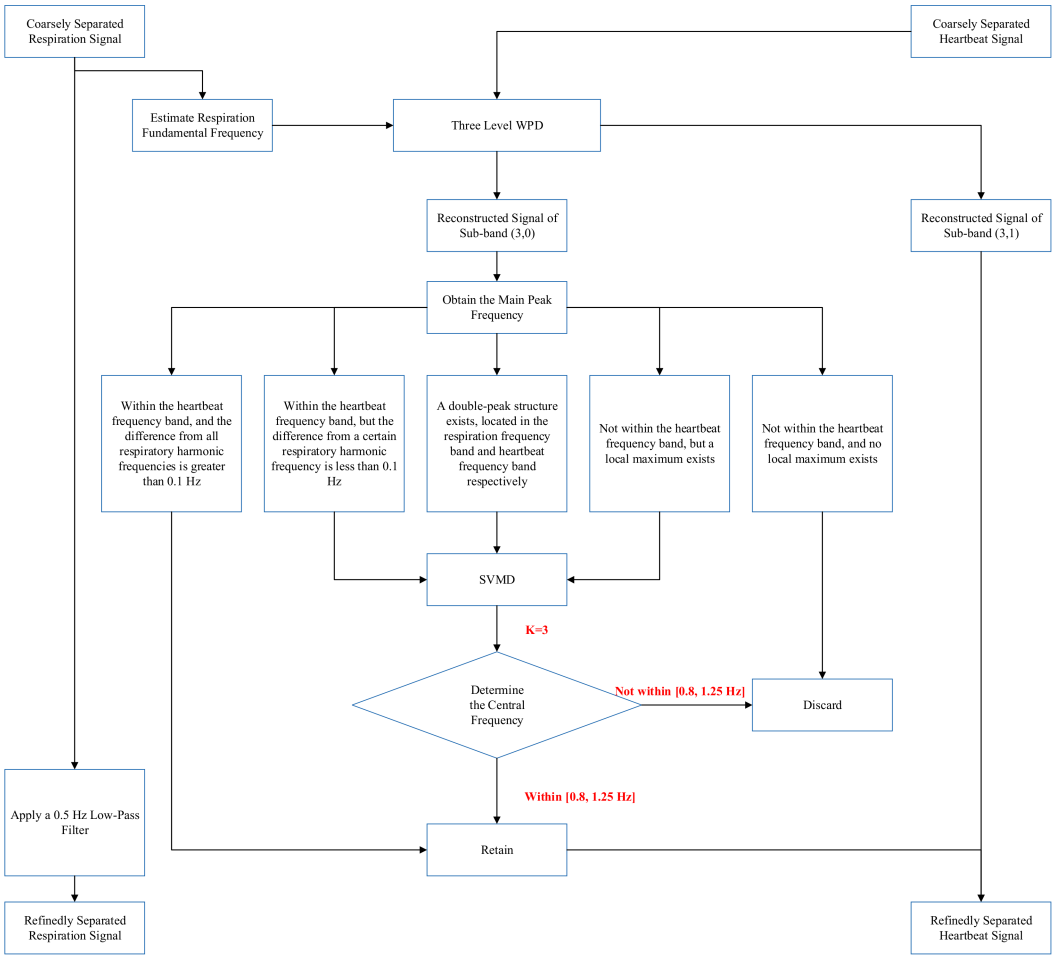


Figure 5. Flowchart of the SVMD Refined Separation Algorithm for Signals.

First, three-layer WPD is performed on the roughly separated heartbeat signal $s'_R(t)$ to obtain wavelet packet coefficients. The heartbeat wavelet packet coefficients are noted as R_j^l, where j $\in [0, 3]$ is the layer number and l $\in [0, 7]$ is the sub-band node number. After WPD, eight sub-bands are obtained. The numbers of each sub-band and their corresponding frequency ranges are shown in Table 3.

Table 3. Frequency ranges of each sub-band after three-layer WPD.

Sub-Band Number	Frequency Range (Hz)	Sub-Band Number	Frequency Range (Hz)
0	0~1.25	4	5~6.25
1	1.25~2.5	5	6.25~7.5
2	2.5~3.75	6	7.5~8.75
3	3.75~5	7	8.75~10

The target frequency band of the heartbeat signal is 0.8~2.5 Hz, spanning sub-band 0 and sub-band 1. Sub-band 0 covers 0~1.25 Hz, and sub-band 1 covers 1.25~2.5 Hz. Thus, sub-bands (3,0) and (3,1) are initially identified as heartbeat reconstruction candidates. However, sub-band 0 also contains part of the low-frequency components (0.8~1.25 Hz) of the respiration and heartbeat signals. Direct superposition of sub-band 0 and sub-band 1 introduces respiration and its high-order harmonic interference into the heartbeat signal. Therefore, components in sub-band (3,0) must be screened.

Although sub-band (3,1) also contains high-order respiratory harmonic components, their energy is relatively low. Even when the heartbeat frequency falls within the range of 1.25–2.5 Hz, the heartbeat signal is much less affected by respiratory high-order harmonics compared with sub-band (3,0). Therefore, the components in sub-band (3,1) are not screened. Taking the measured data of one subject as an example (respiration rate: 18 BPM, heartbeat rate: 76 BPM), the heartbeat spectrum and each respiratory harmonic are shown in Figure 6.

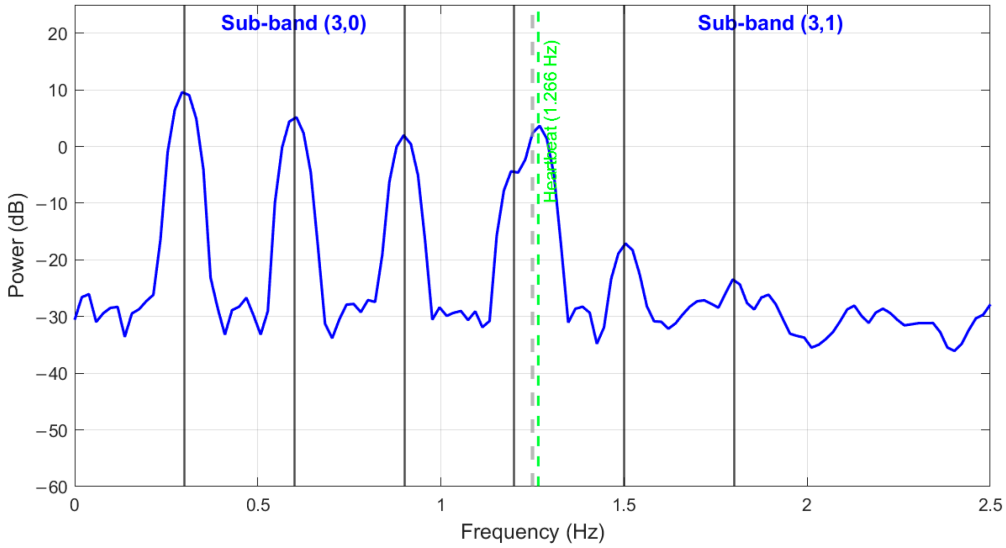


Figure 6. Heartbeat signal spectrum after WPD.

Figure 6 shows the spectrum of the heartbeat signal after WPD and before SVMD processing. As illustrated in the figure, the heartbeat frequency is located in sub-band (3,1). The genuine heartbeat main peak (1.266 Hz) is distinct. The respiratory harmonics within this sub-band exhibit notably diminished energy with increasing order (as clearly observed in the spectrum), and their amplitudes are sufficiently low that they barely affect heartbeat estimation. Therefore, sub-band (3,1) can be directly reconstructed without secondary VMD. However, sub-band (3,0) contains high-energy respiratory harmonics. When the heartbeat main peak falls here, it is prone to being misidentified. Accordingly, secondary VMD is required for sub-band (3,0) to suppress these low-frequency harmonic interferences.

The wavelet packet reconstruction signal of sub-band (3,0) is denoted as $w_0(t)$, Spectrum analysis to obtain its power spectrum $P_0(f)$, and the peak frequency $f_{peak}^{(0)}$ and secondary are first determined. The real-time respiration fundamental frequency f_r is estimated from the roughly separated respiration signal $s'_B(t)$ using peak detection. The respiratory harmonic frequency f'_b satisfies:

$$f'_b = k \cdot f_r, k \in (1, n] \tag{16}$$

where k is an integer.

After obtaining the peak frequency, the following cases are processed:

(1): If the peak frequency is within the heartbeat band (0.8~1.25 Hz) and deviates from all respiratory harmonic frequencies f_b' by more than 0.1 Hz, the peak corresponds to the real heartbeat component, and sub-band (3,0) directly participates in heartbeat reconstruction;

(2): If the peak frequency is within the heartbeat band (0.8~1.25 Hz) but deviates from a respiratory harmonic frequency by less than 0.1 Hz, the heartbeat signal may exist as a secondary peak or be masked by respiratory harmonics. To extract the real heartbeat, SVMD is performed on the wavelet packet reconstruction signal w_0 (t) of sub-band (3,0). The SVMD key parameters [K, α] are set to [3, 2000]. The mode number K = 3 is chosen because sub-band 0 is a narrow-band signal containing only respiration, heartbeat, and a small amount of noise. K = 3 corresponds to three physical sources, fully extracting effective signals while avoiding over-decomposition and false modes when K = 4, and reducing computation. After SVMD, w_0 (t) is split into three narrow-band modes. The mode is screened by central frequency w_k. If $w_k \in$ (0.8 ~ 1.25 Hz) and deviates from all respiratory harmonic frequencies f_b' by more than 0.1 Hz, classify the mode into the heartbeat mode set and discard others. The reconstructed heartbeat component in sub-band (3,0) is:

$$w_0^h(t) = \Sigma_{w_k \in w_H} w_k(t) \tag{17}$$

(3): If a distinct double-peak structure exists (one in respiration band 0.1~0.5 Hz, one in heartbeat band 0.8~1.25 Hz), use SVMD with the same parameters and mode screening rules to obtain the heartbeat component $w_0^h(t)$ in sub-band (3,0).

(4): If the peak frequency is not in the heartbeat band (0.8~1.25 Hz) but a low-amplitude local maximum exists, perform SVMD on the local maximum using the same method.

(5): If no low-amplitude local maximum exists in the spectrum, it is judged that sub-band (3,0) contains no heartbeat component and is discarded.

After three layer WPD and SVMD separation, the obtained heartbeat component $w_0^h(t)$ in sub-band (3,0) is superposed with the reconstruction signal $w_1(t)$ of sub-band (3,1), to obtain the refined heartbeat signal $s_R(t)$:

$$s_R(t) = w_0^h(t) + w_1(t) \tag{18}$$

Notably, the threshold of 0.1 Hz achieves the best performance for distinguishing real heartbeat components from respiratory harmonics. Experiments demonstrate that a smaller threshold (0.05 Hz) may misidentify genuine heartbeat components as harmonics, whereas a larger threshold (0.15 Hz) cannot eliminate interference.

It should be noted that although the 0.1 Hz threshold exhibits optimal performance in most experimental scenarios, this hard-coded threshold may present limitations under complex physiological conditions, such as irregular breathing patterns, arrhythmia, or significantly faster/slower baseline metabolic rates. A more robust approach would be to employ an adaptive thresholding mechanism, which dynamically adjusts the threshold based on the real-time physiological state to enhance adaptability across diverse populations and pathological conditions. In this study, the fixed threshold is adopted as a comprehensive trade-off between computational efficiency and experimental performance, ensuring the algorithm meets the real-time requirements of continuous vital sign monitoring.

Since the respiration signal has strong energy and a single frequency band, it contains almost no interference after rough separation. The refined respiration signal $s_B(t)$ is directly obtained by passing the roughly separated respiration signal $s_B'(t)$ through a 0.5 Hz low-pass filter. Thus, the refined respiration and heartbeat signals after SVMD separation are finally obtained.

4. Experimental Results and Analysis

The hardware system in this paper consists of a millimeter-wave radar sensor and a data acquisition card. The IWR6843ISK millimeter-wave radar sensor, produced by Texas Instruments (TI) (Dallas, TX, USA) and operating in the 60–64 GHz frequency band, is used to transmit electromagnetic waves and receive the echo signals, thereby generating IF signals. The DCA1000EVM data acquisition card is employed to collect the raw IF signals from the radar and transmit them to a PC. On the PC side, MATLAB 2023a is used to process the collected IF signals, and the results are compared with the reference values obtained from a reference instrument. In this experiment, each subject wears a commercial 712T patient monitor manufactured by Wuhan Sichuang Company (Wuhan, China) as the reference device, which has passed the AAMI EC57:2012 standard [18] established by the Association for the Advancement of Medical Instrumentation (AAMI). The experimental setup of this chapter is shown in Figure 7.



Figure 7. Experimental scenario.

The radar parameters are listed in Table 4.

Table 4. Radar parameters.

Parameter	Value
Start frequency/GHz	60
Chirp slope/MHz·μs^{-1}	70
Chirp bandwidth/GHz	4
Chirp period/μs	57
Frame period/ms	50
Number of chirps per frame	1
Number of samples per chirp	200

The IWR6843ISK is equipped with three TX channels and four RX channels. In this study, only one TX channel and one RX channel are used to detect human respiration and heartbeat. For signal processing details, the observation window length is set to 60 s, which provides a frequency resolution of approximately 0.017 Hz. The range-bin is dynamically selected by searching for the peak amplitude in the Range-FFT spectrum corresponding to the subject's chest to ensure the most robust reflection is captured. Phase extraction is performed using the MDACM framework followed by phase unwrapping. Finally, to extract the pure respiration signal, a 4th-order Butterworth low-pass filter with a cutoff frequency of 0.5 Hz is applied.

To systematically evaluate the accuracy and stability of the proposed complete respiration and heartbeat signal separation algorithm, three experimental scenarios are set, and indicators such as accuracy are introduced to evaluate final detection results.

Table 5 lists four experimental scenarios and their descriptions. Three sets of data are collected from six subjects (four males, two females, aged 18~50, no respiratory disease history) For Scenarios ①, ②, and ③, the radial distance between the subject and the radar is fixed at 0.5 m. In Scenario ②, body movement interference mainly consists of standing-sitting motions (frequency ≈ 0.05 Hz) and small-range arm swinging (amplitude: 5–10 cm, frequency ≈ 0.2 Hz). The body movement mainly occurs within 20~40 s. For Scenario ④ (long-distance test), the radial distance is set to 2 m, while keeping all other experimental settings (e.g., subject posture, breathing pattern, and radar parameters) completely identical to Scenario ① to strictly adhere to the single-variable principle.

Table 5. Experimental scenario settings.

No.	Experimental Scenario	Description
①	Static sitting without interference	Subjects sit still in a natural environment
②	Body movement interference	Subjects perform body movements such as arm swinging
③	Complex breathing mode	Subjects perform deep and slow breathing
④	Long-distance measurement	The radial distance between the subject and the radar is increased from 0.5 m to 2 m.

Table 6 lists the evaluation indicators for accuracy and stability. The accuracy D_A is calculated as:

$$D_A = 1 - \frac{\sum_{i=1}^{N} |y_i - x_i|}{\sum_{i=1}^{N} y_i} \times 100\% \quad (19)$$

where x_i is the algorithm estimate of the i experiment, y_i is the actual measured value of the reference device, and $N = 18$ is the number of experiments.

Table 6. Experimental evaluation indicators.

Evaluation Indicator	Description
Accuracy	Evaluates the accuracy of estimation results
Mean Absolute Error (MAE)	Evaluates the stability of estimation results
Bland–Altman analysis [19]	Evaluates the limits of agreement (LOA) between estimated and reference values

MAE measures the average absolute deviation between estimates and reference values, evaluating stability:

$$MAE = \frac{1}{N} \sum_{i=1}^{N} |x_i - y_i| \quad (20)$$

Bland–Altman analysis is a statistical tool for assessing agreement between two measurement methods. It calculates the difference and distribution between measured and reference values to determine the LOA. This paper uses 95% LOA for evaluation: narrower LOA indicates smaller deviation and better agreement between estimates and references. LOA is calculated as:

$$\overline{d} = \frac{1}{N} \sum_{i=1}^{N} (x_i - y_i) \quad (21)$$

$$s = \sqrt{\frac{1}{N-1}\sum_{i=1}^{N}\left(d_i - \overline{d}\right)^2} \tag{22}$$

$$LOA = \left[\overline{d} - 1.96s, \overline{d} + 1.96s\right] \tag{23}$$

where d_i is the difference between x_i and y_i in the i experiment, $\overline{d}$ is the mean of d_i, and s is the standard deviation of differences.

To verify the advantages of the proposed SVMD-based respiration and heartbeat signal separation algorithm, two traditional methods are used for comparison: Band-Pass Filter (BPF) and VMD. The BPF uses passbands 0.1~0.5 Hz (respiration) and 0.8~2.5 Hz (heartbeat). The VMD parameters are set to mode number K = 5 and penalty factor α = 2000. All methods use vector mean subtraction for static clutter removal and peak detection for frequency estimation.

Figures 8–15 show the experimental respiration and heartbeat frequency results of each method under four different experimental scenarios. From the comparison charts under different scenarios, different signal separation methods yield distinct detection performance. The 18 experimental data curves show that BPF and VMD have large deviations, especially in Scenarios ②, ③, and ④; the proposed method closely matches the 712T reference values in all four scenarios, with almost no deviation in Scenario ①. Detailed results are shown in Tables 7–10.

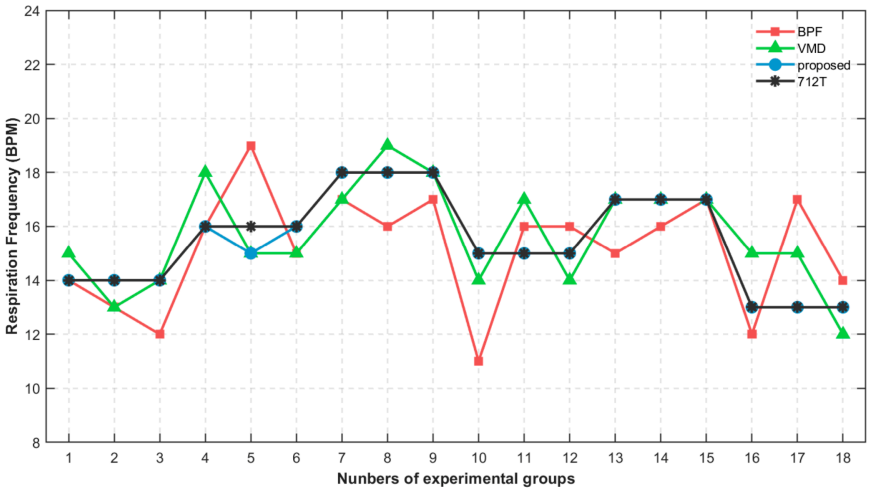


Figure 8. Comparison of respiration results in Scenario ①.

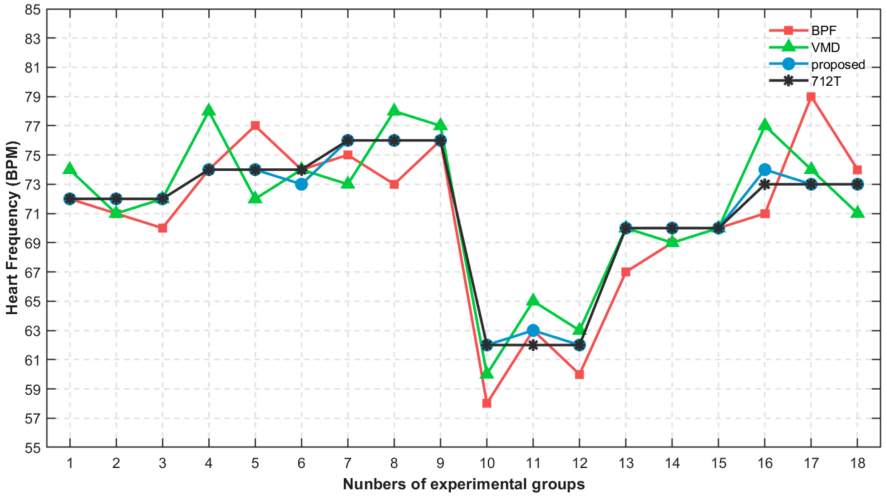


Figure 9. Comparison of heartbeat results in Scenario ①.

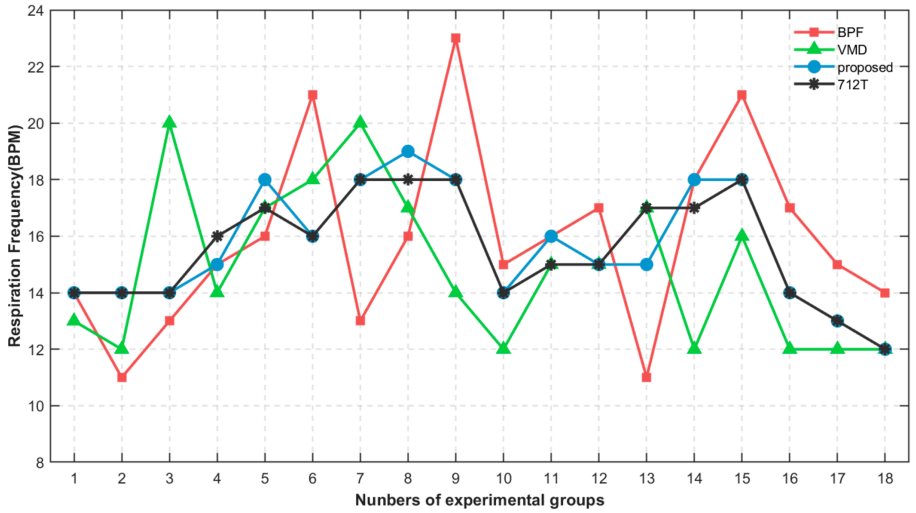


Figure 10. Comparison of respiration results in Scenario ②.

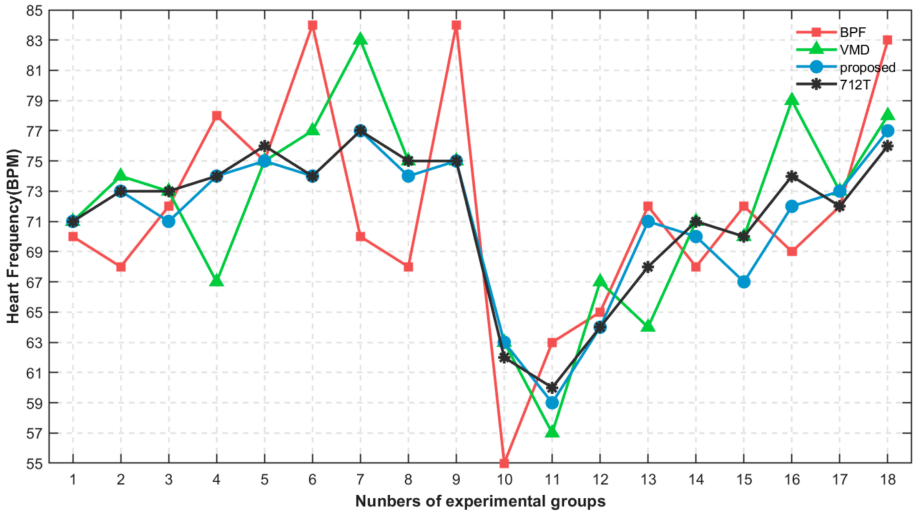


Figure 11. Comparison of heartbeat results in Scenario ②.

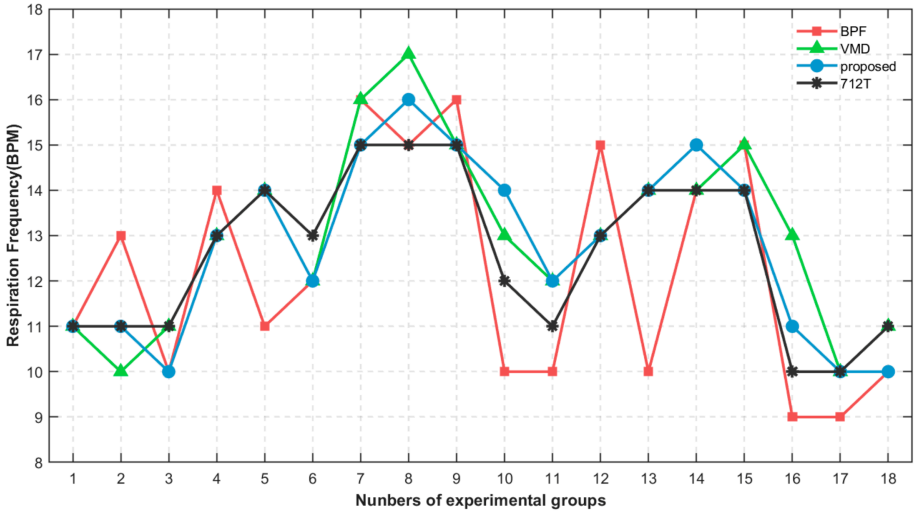


Figure 12. Comparison of respiration results in Scenario ③.

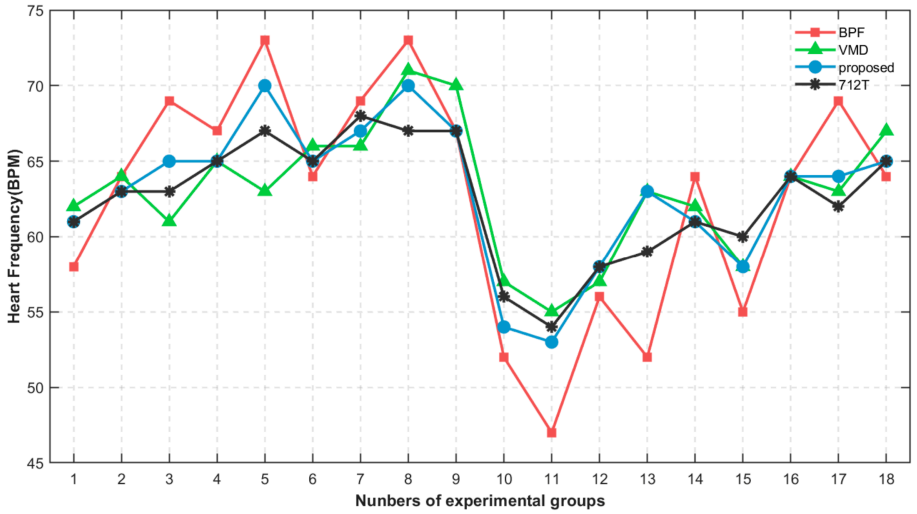


Figure 13. Comparison of heartbeat results in Scenario ③.

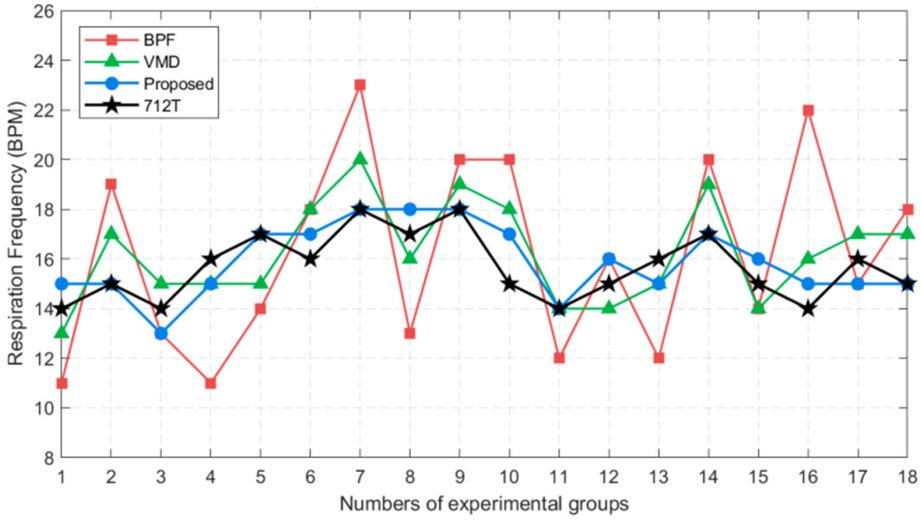


Figure 14. Comparison of respiration results in Scenario ④.

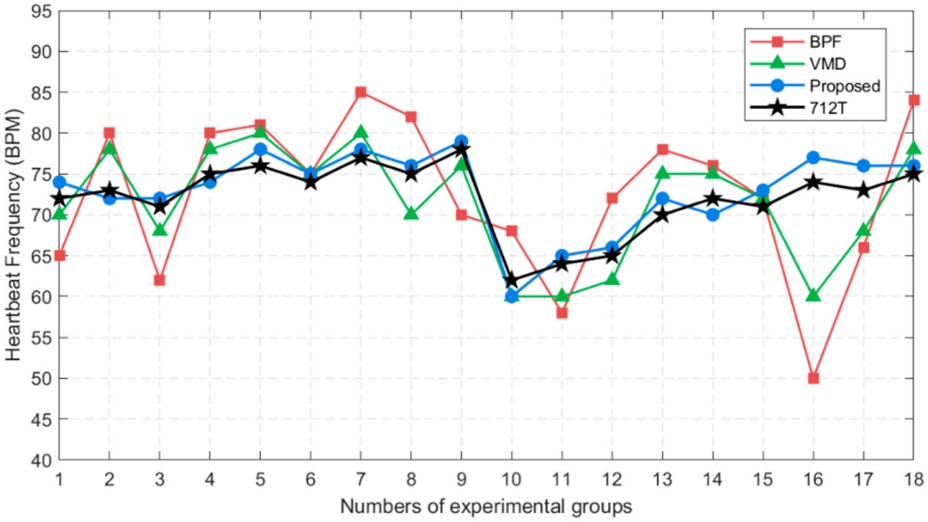


Figure 15. Comparison of heartbeat results in Scenario ④.

Table 7. Experimental results in Scenario ①.

	Respiration Frequency (BPM)				Heartbeat Frequency (BPM)			
No.	**BPF**	**VMD**	**Proposed**	**712T**	**BPF**	**VMD**	**Proposed**	**712T**
1	14	15	14	14	72	74	72	72
2	13	13	14	14	71	71	72	72
3	12	14	14	14	70	72	72	72
4	16	18	16	16	74	78	74	74
5	19	15	15	16	77	72	74	74
6	15	15	16	16	74	74	73	74
7	17	17	18	18	75	73	76	76
8	16	19	18	18	73	78	76	76
9	17	18	18	18	76	77	76	76
10	11	14	15	15	58	60	62	62
11	16	17	15	15	63	65	63	62
12	16	14	15	15	60	63	62	62
13	15	17	17	17	67	70	70	70
14	16	17	17	17	69	69	70	70
15	17	17	17	17	70	70	70	70
16	12	15	13	13	71	77	74	73
17	17	15	13	13	79	74	73	73
18	14	12	13	13	74	71	73	73
accuracy	90.68%	93.90%	99.64%		97.66%	97.73%	99.77%	

Table 8. Experimental results in Scenario ②.

	Respiration Frequency (BPM)				Heartbeat Frequency (BPM)			
No.	**BPF**	**VMD**	**Proposed**	**712T**	**BPF**	**VMD**	**Proposed**	**712T**
1	14	13	14	14	70	71	71	71
2	11	12	14	14	68	74	73	73
3	13	20	14	14	72	73	71	73
4	15	14	15	16	78	67	74	74
5	16	17	18	17	75	75	75	76
6	21	18	16	16	84	77	74	74
7	13	20	18	18	70	83	77	77
8	16	17	19	18	68	74	74	75
9	23	14	18	18	84	74	75	75
10	15	12	14	14	55	63	63	62
11	16	15	16	15	63	57	59	60
12	17	15	15	15	65	67	64	64
13	11	17	15	17	72	64	71	68
14	18	12	18	17	68	71	70	71
15	21	16	18	18	72	70	69	70
16	17	12	14	14	69	79	72	74
17	15	12	13	13	72	73	73	72
18	14	12	12	12	83	78	77	76
accuracy	84.29%	88.57%	97.50%		94.01%	96.96%	98.83%	

Table 9. Experimental results in Scenario ③.

	Respiration Frequency (BPM)				Heartbeat Frequency (BPM)			
No.	**BPF**	**VMD**	**Proposed**	**712T**	**BPF**	**VMD**	**Proposed**	**712T**
1	11	11	11	11	58	62	61	61
2	13	10	11	11	64	64	63	63
3	10	11	10	11	69	61	65	63

Table 9. *Cont.*

	Respiration Frequency (BPM)				Heartbeat Frequency (BPM)			
No.	**BPF**	**VMD**	**Proposed**	**712T**	**BPF**	**VMD**	**Proposed**	**712T**
4	14	13	13	13	67	65	65	65
5	11	14	14	14	73	63	70	67
6	12	12	12	13	64	66	65	65
7	16	16	15	15	69	66	66	68
8	15	17	16	15	73	71	70	67
9	16	15	15	15	67	70	67	67
10	10	14	14	12	52	57	54	56
11	10	12	12	11	47	55	53	54
12	15	13	13	13	56	57	58	58
13	10	14	14	14	52	63	63	59
14	14	14	15	14	64	62	61	64
15	14	15	14	14	55	58	58	60
16	9	13	11	10	64	64	64	64
17	9	10	10	10	69	63	64	62
18	10	11	10	11	64	67	65	65
accuracy	90.31%	94.71%	96.04%		94.77%	97.16%	97.87%	

Table 10. Experimental results in Scenario ④.

	Respiration Frequency (BPM)				Heartbeat Frequency (BPM)			
No.	**BPF**	**VMD**	**Proposed**	**712T**	**BPF**	**VMD**	**Proposed**	**712T**
1	11	13	15	14	65	70	74	72
2	19	17	15	15	80	78	72	73
3	13	15	13	14	62	68	72	71
4	11	15	15	16	80	78	74	75
5	14	15	17	17	81	80	78	76
6	18	18	17	16	75	75	75	74
7	23	20	18	18	85	80	78	77
8	13	16	18	17	82	70	76	75
9	20	19	18	18	70	76	79	78
10	20	18	17	15	68	61	60	62
11	12	14	14	14	58	60	65	64
12	16	14	16	15	72	62	60	65
13	12	15	15	16	78	74	72	70
14	20	19	17	17	76	75	70	72
15	14	14	16	15	72	72	73	71
16	22	16	15	14	50	61	77	74
17	15	17	15	16	66	68	76	73
18	18	17	15	15	84	77	76	75
accuracy	79.79%	90.78%	95.74%		90.05%	95.07%	97.53%	

As shown in Table 7, under Scenario ① (static sitting without interference), the proposed SVMD-based separation algorithm achieves a respiration detection accuracy of 99.64%, which is 8.96 percentage points higher than that of the BPF method and 5.74 percentage points higher than that of the VMD method. The proposed algorithm achieves a heartbeat detection accuracy of 99.77%, which is 2.11 percentage points higher than that of the BPF method and 2.04 percentage points higher than that of the VMD method. According to the quantitative results presented in the table, it can be observed that the proposed algorithm exhibits high accuracy in respiration and heartbeat detection under static, interference-free scenarios, and achieves substantial improvements over traditional signal separation methods (BPF method and VMD method). The comparison results of

respiration and heartbeat detection under complex conditions (Scenario ②, Scenario ③, and Scenario ④) are shown in Tables 8–10.

It can be seen from the respiration and heartbeat detection results in complex and long-distance scenarios in Tables 8–10 that the accuracy of the BPF method decreases significantly, indicating that under these three interference conditions (body movement, complex breathing, and long-distance attenuation), simply relying on manually preset frequency bands achieves poor performance, and the separated signals contain a large amount of clutter interference. Although the VMD method performs better than BPF, its final detection accuracy is still significantly lower than that in Scenario ①. This shows that VMD with manually preset key parameters still retains a large amount of interference components and cannot effectively handle the severely degraded signal-to-noise ratio (SNR) at longer distances. However, the accuracy of the proposed method is consistently better than that of the comparison methods across all scenarios. In Scenario ②, compared with BPF and VMD, the respiration accuracy is improved by 13.21 and 8.93 percentage points, respectively, and the heartbeat accuracy is improved by 4.82 and 1.87 percentage points, respectively. In Scenario ③, the respiration accuracy is improved by 5.73 and 1.33 percentage points, and the heartbeat accuracy is improved by 3.10 and 0.71 percentage points. Notably, in Scenario ④ (2 m distance), where the radar echo energy attenuates severely, the proposed method still maintains an accuracy of 95.74% for respiration and 97.53% for heartbeat. Compared with BPF and VMD, the respiration accuracy is improved by 15.95 and 4.96 percentage points, and the heartbeat accuracy is improved by 7.48 and 2.46 percentage points, respectively. These results prove that the proposed method has high accuracy and strong robustness for final respiration and heartbeat detection even under severe signal attenuation.

Furthermore, to comprehensively evaluate the stability and incorporate recent methodological advancements, two additional baselines are introduced for comparison: Ensemble Empirical Mode Decomposition (EEMD) as a recent adaptive decomposition method [20], and the Cascade Comb Filter (CCF) as a respiratory-harmonic suppression method [21]. The Mean Absolute Error (MAE) results for respiration and heartbeat are presented in Tables 11 and 12.

Table 11. Comparison of MAE results of Respiration Frequency in Different Scenarios.

	Respiration Frequency (BPM)				
	BPF	**VMD**	**EEMD**	**CCF**	**Proposed**
Scenario ①	1.44	0.94	0.62	0.55	0.06
Scenario ②	2.44	1.67	1.32	1.65	0.39
Scenario ③	1.22	0.67	0.65	0.60	0.50
Scenario ④	3.17	1.44	1.15	1.85	0.67

Table 12. Comparison of MAE results of Heartbeat Frequency in Different Scenarios.

	Heartbeat Frequency (BPM)				
	BPF	**VMD**	**EEMD**	**CCF**	**Proposed**
Scenario ①	1.67	1.61	1.15	0.92	0.17
Scenario ②	4.28	2.17	1.70	2.10	0.83
Scenario ③	3.27	1.78	1.35	2.80	1.33
Scenario ④	7.17	3.56	2.85	4.20	1.78

It can be seen from Tables 11 and 12 that the proposed method consistently outperforms all comparison methods across different scenarios, with more obvious improvements

under complex and long-distance conditions (Scenarios ②, ③, and ④). In Scenario ②, compared with BPF, VMD, EEMD, and CCF, the MAE of respiration is reduced by 2.05 BPM, 1.28 BPM, 0.93 BPM, and 1.26 BPM, respectively. This indicates that the proposed method effectively filters out dynamic clutter interference, whereas even the recent EEMD and the harmonic-suppressing CCF struggle due to mode mixing and the lack of dynamic frequency tracking. In Scenario ③, compared with BPF, VMD, EEMD, and CCF, the MAE of heartbeat is reduced by 1.94 BPM, 0.45 BPM, 0.02 BPM, and 1.47 BPM, respectively. Notably, the CCF performs poorly in this complex breathing scenario (MAE = 2.80 BPM) because fixed comb filters cannot track dynamically shifting respiratory harmonics. Furthermore, in Scenario ④ (2 m long-distance test), the overall errors increase due to severe signal attenuation. However, the proposed method still maintains the lowest MAE. Compared with BPF, VMD, EEMD, and CCF, the respiration MAE is reduced by 2.50 BPM, 0.77 BPM, 0.48 BPM, and 1.18 BPM, respectively, and the heartbeat MAE is reduced by 5.39 BPM, 1.78 BPM, 1.07 BPM, and 2.42 BPM. This is because under low signal-to-noise ratio conditions, the fixed-band methods (BPF and CCF) fail to extract weak vital signs, and the decomposition methods (VMD and EEMD) suffer from severe mode mixing. In contrast, the proposed SVMD-based method relies on adaptive parameter optimization and dynamic harmonic tracking to effectively suppress interferences, achieving the lowest MAE and demonstrating strong robustness.

Table 13 shows the 95% Bland–Altman limits of agreement analysis results. It should be noted that the 18 trials were collected from six subjects with three repetitions each. Treating these 18 trials as completely independent samples in the Bland–Altman analysis could potentially introduce pseudo-replication due to intra-subject correlation. To avoid overstating the statistical significance, the Bland–Altman analysis presented in Table 13 is primarily used as a descriptive tool to illustrate the overall limits of agreement between the proposed method and the reference device. We further verified the stability of the method by ensuring that the mean absolute errors for each individual subject remained within a narrow margin. This confirms that the overall consistency is robust and not an artifact of data aggregation or dominated by any single individual.

Table 13. Analysis of Bland–Altman Limits of Agreement Results in Different Scenarios.

Scenarios	Indicator (Beats/Min)	BPF	VMD	Proposed
①	respiration LOA	[−4.02, 3.35]	[−2.19, 2.52]	[−0.52, 0.41]
	heartbeat LOA	[−5.02, 4.02]	[−3.59, 4.25]	[−0.67, 0.67]
②	respiration LOA	[−5.64, 6.31]	[−5.42, 4.09]	[−1.37, 1.48]
	heartbeat LOA	[−10.30, 10.63]	[−5.77, 6.32]	[−2.52, 2.19]
③	respiration LOA	[−5.22, 5.44]	[−1.60, 2.49]	[−1.31, 1.71]
	heartbeat LOA	[−8.52, 8.41]	[−3.97, 4.64]	[−3.55, 4.00]
④	respiration LOA	[−6.78, 7.78]	[−2.47, 3.58]	[−1.50, 1.94]
	heartbeat LOA	[−16.83, 17.61]	[−9.48, 8.15]	[−3.43, 4.55]

It should be noted that the ±2 BPM and ±5 BPM thresholds adopted in this study are not direct clauses of AAMI EC57:2012 (which focuses on arrhythmia and ST-segment algorithms), nor are they equivalent to the measurement accuracy criteria specified in AAMI EC13 (which requires the device's heart rate error to be within ±5 BPM or ±10%). Instead, these thresholds correspond to clinically acceptable limits of agreement (LOA) widely used in vital-sign monitoring literature for evaluating the overall statistical consistency between a new method and a reference device.

Combined with the results in Table 13, the BPF and VMD methods fail to meet these criteria in multiple scenarios (e.g., the heartbeat LOA of VMD exceeds ±5 BPM in Scenarios ② and ③). Furthermore, in Scenario ④ (2 m long-distance), due to severe signal attenuation and low SNR, the heartbeat LOAs of BPF and VMD degrade drastically to $[-16.83, 17.61]$ and $[-9.48, 8.15]$, respectively, both significantly exceeding the ±5 BPM threshold. In contrast, the proposed method maintains a narrow heartbeat LOA of $[-3.43, 4.55]$ and a respiration LOA of $[-1.50, 1.94]$. Thus, the proposed method satisfies the clinically referenced AAMI device accuracy expectations across all scenarios, including complex and long-distance conditions, and significantly outperforms the other two methods. This indicates that the proposed SVMD-based separation algorithm yields small deviations from the reference values and good consistency, with stronger stability than BPF and VMD. Admittedly, as we collected three trials per subject from six participants, minor result discrepancies may arise inevitably from intra-subject dependence. We acknowledge this limitation of our dataset.

To evaluate the individual contribution of each module in the proposed method, an ablation study is conducted. The complete algorithm consists of three key stages: GWAIVMD, WPD, and SVMD. The MAE results for different module combinations under complex scenarios are shown in Table 14.

Table 14. Respiration and heartbeat results of ablation study under complex scenarios (MAE in BPM).

Scenario	Vital Sign	VMD	GWAIVMD	GWAIVMD + WPD	Proposed
Scenario ②	Respiration	1.67	1.21	0.82	0.39
	Heartbeat	2.17	1.45	0.98	0.83
Scenario ③	Respiration	0.67	0.65	0.52	0.50
	Heartbeat	1.78	1.48	1.32	1.33
Scenario ④	Respiration	1.44	0.98	0.75	0.67
	Heartbeat	3.56	2.35	1.95	1.78

As shown in Table 14, switching from the baseline VMD to GWAIVMD significantly reduces the MAE of the final results (e.g., the heartbeat MAE in Scenario ② decreases from 2.17 to 1.45 BPM), which demonstrates the effectiveness of GWAIVMD in avoiding under-decomposition and over-decomposition. After introducing WPD, the separation performance is further improved by accurately separating the respiration and heartbeat bands, and purer signals are obtained. Finally, SVMD is introduced to suppress the residual high-order respiratory harmonics, and the complete method achieves the lowest MAE. Notably, in Scenario ③, the SVMD stage plays a critical role, reducing the heartbeat MAE from 1.48 BPM to 1.33 BPM. Furthermore, in Scenario ④ (2 m distance), although the overall errors increase due to signal attenuation, the MAE still exhibits a clear stepwise decline (e.g., heartbeat MAE decreases from 3.56 to 1.78 BPM) as the modules are progressively added. This proves that the adaptive parameter optimization (GWAIVMD) and refined separation (WPD+SVMD) are highly robust in dealing with both complex interference and severe signal attenuation. The ablation results verify that each module of the proposed cascaded algorithm contributes positively to the robustness of the final results.

5. Conclusions

This paper proposes a respiration and heartbeat signal separation algorithm based on SVMD to suppress clutter interference and the influence of respiratory high-order harmonics in FMCW radar detection. The algorithm first coarsely separates the phase signal through GWAIVMD, and then performs refined separation through WPD and SVMD, finally obtaining purer respiration and heartbeat signals. Experimental results show that

the proposed SVMD-based algorithm achieves a detection accuracy of more than 95.59% in four experimental scenarios, and the MAE of respiration and heartbeat is lower than other methods, including BPF, VMD, EEMD, and CCF, which proves the strong stability of the proposed method. The 95% Bland–Altman limits of agreement show that the detection results meet the clinically referenced AAMI device accuracy expectations across all scenarios. These results provide strong support for non-contact respiration and heartbeat detection using FMCW millimeter-wave radar.

However, the proposed algorithm still has certain limitations. First, the experimental data are collected from only six subjects, lacking a large number of clinical samples. Second, the current system is validated in a single-subject scenario. In real-world applications such as home monitoring or hospital wards, multiple targets may coexist. In such multi-target scenarios, the echoes from different human bodies can easily overlap in the same range bin. Since the proposed GWAIVMD and SVMD pipelines rely purely on frequency-domain separation, they struggle to decouple the vital signs if two subjects have overlapping respiratory or heartbeat frequencies, or if mutual body movements cause severe spectral aliasing. In future work, data-driven methods such as deep learning can be combined with signal separation algorithms to cope with more extreme scenarios. Furthermore, multiple-input multiple-output (MIMO) radar with spatial beamforming or blind source separation techniques can be explored to achieve spatial separation of multiple targets before applying our method. Cooperation with hospitals will also be sought to provide more experimental data of people of different ages and health conditions, so as to evaluate the universality and clinical applicability of the method.

Author Contributions: Conceptualization, Z.Y., Y.Y., Q.C., and X.W.; Methodology, Z.Y. and X.W.; Software, Z.Y. and Y.C.; Validation, Z.Y.; Formal analysis, Y.Y.; Investigation, Y.Y. and Q.C.; Resources, Y.C. and Q.C.; Data curation, Z.Y.; and Q.C.; Writing—original draft, Z.Y.; Writing—review and editing, Z.Y., Y.C., Q.C., and X.W. All authors have read and agreed to the published version of the manuscript.

Funding: This research was funded by the National Natural Science Foundation of China (NSFC), grant number 82427801.

Institutional Review Board Statement: The study was conducted in accordance with the Declaration of Helsinki. Ethical review and approval were waived for this study based on the national guidelines for ethical review of life sciences and medical research involving human subjects (2023). This exemption was justified because the study involved only non-invasive, non-contact radar sensing of anonymous vital signs from healthy volunteers, without any physical intervention, collection of biological samples, or sensitive personal information. All subjects provided informed consent prior to the experiments.

Informed Consent Statement: Informed consent was obtained from all subjects involved in the study.

Data Availability Statement: The data presented in this study are available on request from the corresponding author due to the fact that the data were collected personally and involve the privacy of the subjects, so they cannot be made publicly available.

Conflicts of Interest: The authors declare no conflicts of interest.

Abbreviations

The following abbreviations are used in this manuscript:

AAMI	Association for the Advancement of Medical Instrumentation
BPF	Band-Pass Filter
CCF	Cascaded Comb Filter
CW	Continuous Wave
DSP	Digital Signal Processor

EEMD	Ensemble Empirical Mode Decomposition
EMD	Empirical Mode Decomposition
FMCW	Frequency Modulated Continuous Wave
GWA	Grey Wolf Algorithm
GWAIVMD	Grey Wolf Algorithm Improved Variational Mode Decomposition
IF	Intermediate Frequency
IMF	Intrinsic Mode Function
LOA	Limits of Agreement
MAE	Mean Absolute Error
Range-FFT	Range-Dimensional Fast Fourier Transform
RX	Receive Antenna
SVMD	Secondary Variational Mode Decomposition
SVD	Singular Value Decomposition
TX	Transmit Antenna
UWB	Ultra-Wide Band
VMD	Variational Mode Decomposition
WD	Wavelet Denoising
WPD	Wavelet Packet Decomposition

References

1. World Health Organization. *Clinical Management of COVID-19: Living Guideline*; WHO: Geneva, Switzerland, 2023.
2. Kr, B.A.; Zhang, X.; Chityat, I.; Brady-Mine, A.; Linton, E.; Copeland, D.; Anthony, B.W.; Edelman, E.R.; Davis, J.M. Emerging innovations in neonatal monitoring: A comprehensive review of progress and potential for non-contact technologies. *Front. Pediatr.* **2024**, *12*, 1442753. [CrossRef]
3. Zhang, Y.; Huang, Y.; Huang, M. Research progress on non-contact vital signs monitoring technology. *Acta Electron. Sin.* **2023**, *51*, 1756–1772. (In Chinese)
4. Wang, J.; Li, L.; Liu, C. Current status and popularization barriers of vital signs monitoring equipment in primary healthcare institutions. *China Med. Devices* **2022**, *37*, 145–148. (In Chinese)
5. Fang, Z.; Jian, P.; Zhang, H.; Yao, Y.; Geng, F.; Liu, C.; Yan, B.; Wang, P.; Du, L.; Chen, X. Review of non-contact healthcare monitoring technology based on FMCW radar. *J. Radars* **2022**, *11*, 499–516. (In Chinese)
6. Wang, D.; Yoo, S.; Cho, S.H. Experimental comparison of IR-UWB radar and FMCW radar for vital signs. *Sensors* **2020**, *20*, 6695. [CrossRef]
7. Lin, J.C.; Kiernicki, J.; Kiernicki, M.; Woll, J. Microwave apexcardiography. *IEEE Trans. Microw. Theory Tech.* **1979**, *27*, 618–620. [CrossRef]
8. Xu, Z.W.; Liu, T. Vital sign sensing method based on EMD in terahertz band. *EURASIP J. Adv. Signal Process.* **2014**, *2014*, 75. [CrossRef]
9. Dragomiretskiy, K.; Zosso, D. Variational mode decomposition. *IEEE Trans. Signal Process.* **2014**, *62*, 531–544. [CrossRef]
10. Islam, S.M.M.; Boric-Lubecke, O.; Lubecke, V.M. Vital signs monitoring using Doppler radar based on variational mode decomposition. In Proceedings of the 2015 IEEE MTT-S International Microwave Workshop Series on RF and Wireless Sensors, Taipei, Taiwan, 1–3 July 2015; pp. 1–4.
11. Qu, L.; Liu, C.; Yang, T.; Sun, Y. Vital Sign Detection of FMCW Radar Based on Improved Adaptive Parameter Variational Mode Decomposition. *IEEE Sens. J.* **2023**, *23*, 25048–25060. [CrossRef]
12. Liu, Z.; Li, C.; Wang, Z. A cascaded singular spectrum analysis for interference suppression of millimeter wave bioradar in vital sign detection. *Biomed. Signal Process. Control* **2025**, *100*, 106929. [CrossRef]
13. Wu, J.; Dahnoun, N. A health monitoring system with posture estimation and heart rate detection based on millimeter-wave radar. *Microprocess. Microsyst.* **2022**, *94*, 104670. [CrossRef]
14. Oppenheim, A.V.; Schafer, R.W.; Buck, J.R. *Discrete-Time Signal Processing*, 2nd ed.; Prentice Hall: Upper Saddle River, NJ, USA, 1999; p. 561.
15. Gray, D.J. Cramér-Rao bounds for range and Doppler estimation with a linear FM pulse. *IEEE Trans. Aerosp. Electron. Syst.* **1990**, *26*, 221–227.
16. Coifman, R.R.; Wickerhauser, M.V. Entropy-based algorithms for best basis selection. *IEEE Trans. Inf. Theory* **1992**, *38*, 713–718. [CrossRef]
17. Xie, H.; Liu, Y.; Jin, M.; Xia, B. EEG signal wavelet processing based on DSP Builder. *Electron. Des. Eng.* **2009**, *17*, 76–79. (In Chinese)

18. *ANSI/AAMI EC57:2012/(R)2020*; Testing and Reporting Performance Results of Cardiac Rhythm and ST Segment Measurement Algorithms. AAMI: Arlington, VA, USA, 2012.
19. Bland, J.M.; Altman, D.G. Statistical methods for assessing agreement between two methods of clinical measurement. *Lancet* **1986**, *327*, 307–310. [CrossRef]
20. Wu, Z.; Huang, N.E. Ensemble empirical mode decomposition: A noise-assisted data analysis method. *Adv. Adapt. Data Anal.* **2009**, *1*, 1–41. [CrossRef]
21. Huang, T.-Y.; Hayward, L.; Lin, J. Adaptive harmonics comb notch digital filter for measuring heart rate of laboratory rat using a 60-GHz radar. In Proceedings of the 2016 IEEE MTT-S International Microwave Symposium (IMS), San Francisco, CA, USA, 22–27 May 2016; pp. 1–4.

Disclaimer/Publisher's Note: The statements, opinions and data contained in all publications are solely those of the individual author(s) and contributor(s) and not of MDPI and/or the editor(s). MDPI and/or the editor(s) disclaim responsibility for any injury to people or property resulting from any ideas, methods, instructions or products referred to in the content.